Performance Bounds for Sinogram Decomposition and Potential Benefits of Multi-energy Data

Yaoshen Yuan
Department of Electrical and Computer Engineering
Tufts University
Medford, MA 02155 USA
Email: yaoshen.yuan@tufts.edu

Brian Tracey
Department of Electrical and Computer Engineering
Tufts University
Medford, MA 02155 USA
Email: btracey@eecs.tufts.edu

Eric Miller
Department of Electrical and Computer Engineering
Tufts University
Medford, MA 02155 USA
Email: elmiller@ece.tufts.edu

***Abstract*—X-ray inspection plays an important role in materials identification for airline security. Switched dual-energy (SwDE) systems allow material identification by reconstructing the Compton and photoelectric (PE) coefficients of scanned objects, but dual-energy system performance can be strongly impacted by metal or other highly attenuating materials. Here we study the potential benefits of using multi-energy photon counting detectors to reconstruct the Compton and PE coefficients. Using simulations that employ a modified sinogram decomposition algorithm and reconstructing images after sinogram decomposition, we see that utilizing measurements from a small (< 10) number of bins can noticeably improve performance compared to two bins, in particular when metal is present. In order to understand fundamental performance limits, we carried out theoretical calculations of SNR upper bound based on Cramér Rao lower bound (CRLB) variance estimates. In our parameter study we consider several materials (aluminum and nylon) for objects of varying lengths. The CRLB results show general agreement with our algorithmic reconstructions, confirming that multi-energy measurements appear to be beneficial. Overall, our results suggest that further investigation of multi-energy detectors for airline screening applications is warranted.**

I. Introduction

As terrorism has increasingly threatened aviation security, airport baggage scanning using X-rays or other technologies has become increasingly important. The geometric information provided by CT provides important cues for understanding the bag contents. Materials identification using only the estimated attenuation is possible, but dual- or multi-energy systems can provide additional cues for material identification. Thus, Ying *et al.* proposed a two-step dual-energy CT (DECT) process in which sinogram decomposition is first used to estimate Compton and photoelectric (PE) coefficient sinograms, after which each sinogram is reconstructed [1].

While dual-energy methods can provide valuable new information, the results can be severely corrupted when metal or other highly attenuating objects are present. We seek to understand whether multi-energy CT (MECT) using photon counting detectors can help this problem. As described below, our simulation work shows that a multi-energy extension of [1] shows that a multi-energy method can recover Compton and PE coefficients even in a challenging case where metal artifacts cause a dual-energy method to fail. We find that, even though only two quantities (Compton and PE) are estimated, benefits are seen by including up to 5-10 energy bins.

An important question is whether this improvement reflects differences in the solution methods used, or a fundamental difference in the information available with MECT vs. DECT. Therefore, we calculate theoretical performance bounds using the Cramér Rao lower bound (CRLB), varying the number of energy bins as well as material properties of objects being imaged. This result gives us a theoretical upper limit of SNR that any algorithm can achieve. Therefore, this approach provides a general way to predict the SNR trends. As shown below, the CRLB analysis supports the idea that the multiple energy bins help improve the reconstruction.

In a classic paper, Alvarez and Macovski [2] computed the CRLB for dual-energy sinogram decomposition. They considered the situation where only two individual energy bins are used and the bins have perfect energy resolution. Their work was extended to multi-energy bins by Roessl and Herrmann [3] who modeled both photon-counting detector systems and energy-integrating detector systems, and furthermore account for the imperfect energy resolution of photon-counting systems (modeling overlap between energy bins). We build on this work but assume that only photon counting detectors are used for MECT.

The structure of this paper is as follows. In the next section, we review the CRLB bounds calculation for multi-energy sinogram decomposition. In the Results section, we briefly describe our simulation results (which using a weighted multi-energy decomposition method) and then compare trends from simulations to trends computed using CRLB. Finally, we conclude and suggest directions for future work.

II. Performance Bound Calculation

In this section, the CRLB is used to derive both variance and SNR of A_c and A_p [4][5].Because here we only use photon counting detectors to measure the number of photons falling into each energy bin, no Gaussian noise will be added to our model. Simplifying the results of Roessl and Herrmann [3] to consider only photon counting detectors, the likelihood

function given can be described as the product of Poisson distributions for each bin (Eq.1).

$$P(I_1, I_2, \ldots, I_M | A_c, A_p) = \prod_{i=1}^{M} \frac{\lambda_i^{I_i}}{I_i!} e^{-\lambda_i} \tag{1}$$

where I_i is the photon counts detected at the ith bin and M is the number of bins, A_c and A_p are the values of the Compton and Photoelectric sinogram for a given ray path, and λ_i is the expected number of counts in the ith energy bin. The number of counts is a function of two given estimates A_c and A_p, and is modeled as:

$$\lambda_i(A_c, A_p) = \int S_i(E) e^{-A_c f_{KN}(E) - A_p f_p(E)} dE \tag{2}$$

where $S_i(E)$ is the spectrum for ith bin. We can simulate the spectra for MECT using the model in [3], which models the energy resolution caused by the photon counting detectors, accordingly for imperfect energy resolution (see [3] for details). Then the log-likelihood can be written as

$$L = lnP(I_1, I_2, \ldots, I_M | A_c, A_p) = \sum_{i=1}^{M} [I_i ln\lambda_i - \lambda_i - ln(I_i!)] \tag{3}$$

We assume the parameter vector is $\theta = [Ac, Ap]^T$. The Fisher information matrix with respect to A_c and A_p is

$$I(\theta) = \begin{bmatrix} F_{cc} & F_{cp} \\ F_{pc} & F_{pp} \end{bmatrix} \tag{4}$$

Each element in the matrix is

$$F_{\alpha\beta} = F_{\beta\alpha} = -E\left[\frac{\partial^2 L}{\partial A_\alpha \partial A_\beta}\right] = \sum_{i=1}^{M} \frac{1}{\lambda_i}\left(\frac{\partial \lambda_i}{\partial A_\alpha}\right)\left(\frac{\partial \lambda_i}{\partial A_\beta}\right) \tag{5}$$

where α and β are a notational shorthand and can represent either c and p. Then inverting the Fisher information matrix $I(\theta)$ yields

$$I^{-1}(\theta) = \frac{1}{det(I(\theta))} \begin{bmatrix} F_{pp} & -F_{cp} \\ -F_{pc} & F_{cc} \end{bmatrix} \tag{6}$$

We know that $var(\hat{\theta}_i) \geq \left[\boldsymbol{I}^{-1}(\boldsymbol{\theta})\right]_{ii}$ [4], so CRLBs for A_c and A_p are

$$var(\hat{A}_c) = \sigma^2_{A_c} \geq \frac{1}{det(I(\theta))} F_{pp} = \frac{1}{det(I(\theta))} \sum_{i=1}^{M} \frac{1}{\lambda_i}\left(\frac{\partial \lambda_i}{\partial A_c}\right)^2$$
$$var(\hat{A}_p) = \sigma^2_{A_p} \geq \frac{1}{det(I(\theta))} F_{cc} = \frac{1}{det(I(\theta))} \sum_{i=1}^{M} \frac{1}{\lambda_i}\left(\frac{\partial \lambda_i}{\partial A_p}\right)^2 \tag{7}$$

The lower bound of variance is shown in Eq.7, so the upper bound of SNR given A_c and A_p is

$$SNR_{Ac} \leq \frac{A_c}{\sigma_{A_c}}$$
$$SNR_{Ap} \leq \frac{A_p}{\sigma_{A_p}} \tag{8}$$

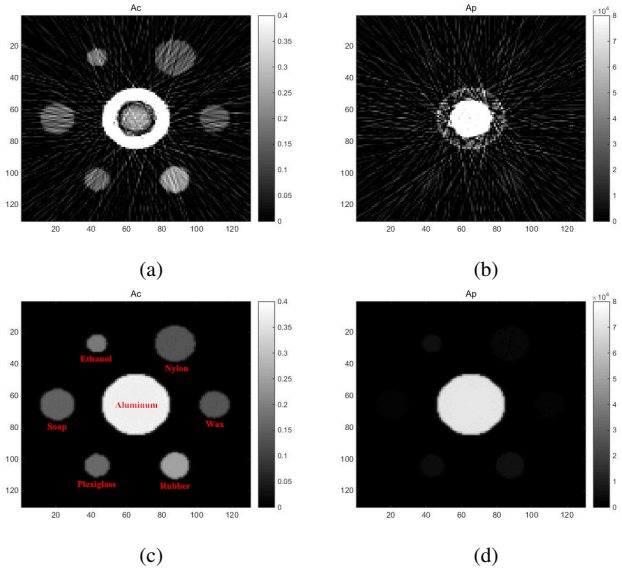

Fig. 1: Simulation for a phantom with high attenuation (aluminum center). First row: reconstructions using SwDE. Second row: reconstruction using MECT with 7 bins. Compton images are in the left column with PE in the right column.

Below we express SNR in decibels. For raypath k, A_c, A_p are given by the line integral through any objects along that raypath of either Compton coefficients or PE coefficients. We can learn from Eq.5 that the SNR upper bound is a function of A_c, A_p and M. In the following sections, we will explore the relationship between these three variables and compare the results to the realistic simulations of different attenuations.

III. Results

To simulate the Compton and PE reconstructions, we construct a phantom with aluminum in the middle, which has a high attenuation (labels in Fig. 1c). We simulated data for a switched dual-energy system (SwDE), in which the object is scanned twice using different spectra (spectrum are taken from [6] and integrating detectors are used (here we do not model additive Gaussian noise for the SwDE detectors, which would degrade SwDE performance). We also simulate performance for the same phantom using a multi-energy (7 bin) approach, by extending the work of Ying *et al.* to the multi-energy case and also weight the data for different bins by the number of counts. The optimization problem solved is:

$$(\theta^k) = \arg\min_{\theta^k} (\boldsymbol{K}(\boldsymbol{\theta^k}) - \boldsymbol{m^k})^T \boldsymbol{\Sigma} (\boldsymbol{K}(\boldsymbol{\theta^k}) - \boldsymbol{m^k}) \tag{9}$$

where θ^k=$\left[A_c^k, A_p^k\right]$ are the estimated quantities for ray k, $\boldsymbol{K}$ is the forward model, $\boldsymbol{K}(\theta^k)$ is the *estimated M* dimensional column vector of log-normalized mean values, and $\boldsymbol{m^k}$ is the data, as a *M* dimensional column vector of log-normalized measured projections. The weighting term is given by $\boldsymbol{\Sigma}$=diag$\{\boldsymbol{w}\}$ where w is the number of counts. This weighting term is found from a quadratic approximation to likelihood function and was proposed by Bouman for CT

reconstruction [7]. This weighting was found to noticeably improve performance. For both SwDE and MECT, after the data are decomposed into Compton and photoelectric coefficients, filtered backprojection (FBP) method is used to reconstruct the images shown in Fig. 1c.

Fig. 1 shows that the reconstruction using multi-energy bins (7 bins) can noticeably improve the PSNR of both Compton and PE images compared to the SwDE. Artifacts in both Compton and PE images are obviously reduced by using MECT with the proposed weighted multi-energy solution.

Fig. 1 shows results for a single phantom and a single realization. We carried out further simulations for phantoms with high, medium and low attenuation, and averaging across realizations, to study how the number of bins influences image domain results. We computed the PSNR of Compton and PE reconstructions utilizing Eq.9. Here we use a unified peak signal value to calculate the PSNR for all three phantoms, which is the true Compton and PE coefficients of aluminum (0.37 $\text{KeV}^3\text{cm}^{-1}$ and 72440 cm^{-1} respectively). Moreover, the phantom with medium attenuation is the same as Fig. 1c but the aluminum is replaced by cotton and ethanol is replaced by aluminum; the phantom with low attenuation is also Fig. 1c but only aluminum is substituted by cotton. Similar to the calculations of SNR upper bounds, we reconstructed the Compton and PE images using both MECT and SwDE within the range of 2 to 10 energy bins. For each point, we obtain the PSNR by taking the average of 30 calculations. The results are shown in Fig. 2. The circles in the figure represent the PSNR of SwDE. We can notice that the PSNR of high attenuation is obviously lower than the PSNRs of medium and low attenuation. This is close to the result of SNR upper bound, where the SNR upper bound decreases with the increasing length of material. Fig. 2 also shows that the increment of the number of bins can slightly improve the PSNR. For Compton and PE images, the improvement caused by MECT is observable when the bin number is less than 5, but the PSNR becomes flat with continuous increase of bin number, which shows a trend similar to the SNR upper bounds. Furthermore, the improvement is not apparent for the phantom with high attenuation. This is result from the relatively high mean square error (MSE) of the reconstructions with high attenuation since MSE is the denominator of PSNR. Fig. 2 also presents the PSNR obtained by using SwDE. The PSNR of SwDE is much lower than MECT with 2 energy bins. Over 20 dB improvement can be seen for all three phantoms. The result demonstrates a significant benefit of using MECT in reconstructing Compton and PE images in contrast with SwDE.

CRLB RESULTS: As a next simulation step, we used the CRLB calculations described previously to study the SNR upper bounds with respect to the number of bins as well as the length and type of material along a raypath. In the simulation, we calculated the SNR upper bound for 2 bins to 10 bins. For each bin, we used the model of Roessl and Herrmann where realistic energy resolution is considered to obtain the spectrum [3]. We also compare the SNR upper

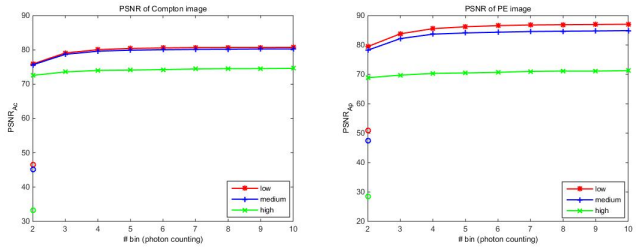

(a) (b)

Fig. 2: Image domain: PSNR (Peak SNR) of both Compton and PE image reconstructed by the weighted method using photon counting detector (weighted MECT), as a function of number of energy bins. The circles in the figure represent the weighted SwDE method. The results demonstrate that the PSNR of weighted SwDE method is much lower than the weighted MECT.

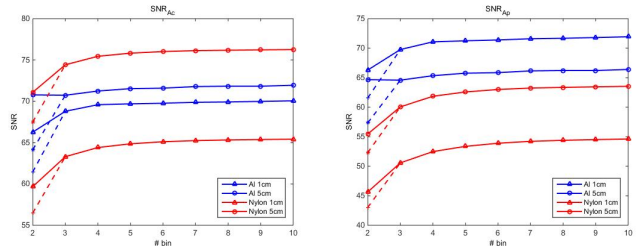

(a) (b)

Fig. 3: Sinogram domain: CRLB-predicted SNR upper bounds for aluminum and nylon. The solid lines indicate the MECT; the dashed lines indicate the SwDE

bound for SwDE using integrating detectors to MECT using photon counting detectors. The asterisks connected by dashed lines in Fig. 3 indicate the SNR upper bounds generated by SwDE. Because the SNR upper bound is a function of the amount of attenuation and the number of energy bins, for each bin number, we simulated different lengths of material. Here we choose 1 cm, 5 cm and 10 cm, which cover a range that reflects how the length influences the SNR upper bound.

In this section, we also study the effects of material attenuation, using aluminum and nylon as examples of high- and low-attenuation materials. The Compton and PE coefficients for aluminum are 0.37 $\text{KeV}^3\text{cm}^{-1}$ and 72440 cm^{-1} respectively. The Compton and PE coefficients for nylon are 0.1325 $\text{KeV}^3\text{cm}^{-1}$ and 2771 cm^{-1} respectively. Thus the SNR upper bounds for these two materials can be used to provide useful information how material attenuation affects the reconstructions.

In work not shown here, we also computed the SNR upper bound for MECT with perfect energy resolution ('ideal MECT'), which means each bin is ideally resolved without energy overlap. The result shows almost no difference in CRLB predictions between the SNR upper bound of MECT using Roessl's model and the upper bound of ideal MECT.

As shown in Fig. 3, for MECT using photon counting

TABLE I: The predicted SNR (in decibels) for upper bounds of 2 bins and 3 bins, modeling ray paths passing through aluminum. While Fig. 3 assumes that all energy bins have equal size in keV, the results shown here were found by a brute force search to find optimal, unequal bin sizes

	Compton		photoelectric	
	2 bins	3 bins	2 bins	3 bins
5 cm	71.03	71.56	64.99	65.78
10 cm	65.71	66.30	55.68	56.64

detector the number of bins has a positive effect on the SNR upper bound when the bin number is small. The SNR upper bound shows little increase as the number of bins increases beyond 5 bins. However, we can observe that the SNR of 2 bins using MECT is higher than the SNR of 3 bins for the case of 5 cm aluminum. While this appears counter-intuitive, it is explained because our calculation assumed that energy band are divided into equal keV ranges, which may not be ideal. If we instead tune to find the optimal separator of energy ranges (instead of splitting the energy range into 2 or 3 equal bins), we can see from Table I that the best SNR upper bound for 3 energy bins is slightly better than the one for 2 energy bins, as expected. This suggests that unequal energy bin spacing may be of some value.

Unlike aluminum, the improvement of nylon is more noticeable as the number of bins increases, but the improvement becomes increasingly small as the number of bins grows beyond 5 bins. As we can see, the SNR upper bound of SwDE, which is indicated by the dashed lines in Fig. 3, is much lower than MECT for both aluminum and nylon. Considering that SwDE employs integrating detectors which generate Gaussian noise (which we are not including in calculations) in addition to Poisson noise [8], the improvement made by MECT in reality may be understated, showing the potential of using MECT for realistic Compton and PE reconstructions.

In addition, the variance of SNR upper bound also depends on the length of material. For both Compton and PE coefficients, when the length is small (1 cm), the upper bound of aluminum is higher than nylon. With the increasing length of materials, the SNR upper bound of aluminum becomes lower than the upper bound of nylon. Our simulation of the SNR upper bound with respect to the length of materials shows that the SNR of aluminum drops much faster than nylon as the length increases, which demonstrates that the SNR of aluminum is more sensitive to the changing length.

IV. Conclusion

In this paper, we presented both simulation results and theoretical performance bounds for dual-energy and multi-energy systems, assuming a sinogram decomposition method is used to decompose data in Compton and photoelectric coefficients. We first reviewed for CRLB computation for multi-energy using photon counting detectors. We then presented both image-domain simulation results and sinogram-domain performance predictions for switched dual-energy and multi-energy systems. The results show that the trend of for simulated performance (PSNR) is similar to the predicted theoretical SNR upper bound. Increasing number of bins can improve the PSNRs of reconstructions regardless of the attenuation of material, though gains become limited as the number of bins increases. In both sets of results, multi-energy performance was better than switched dual-energy, showing the promise of MECT for the Compton and PE reconstructions.

The work shown in this paper is based on a combination of simulated data and performance bound calculation. Our future work will be focused on attempting to demonstrate these gains using experimental data, studying various phantoms. We will study whether or not use of multiple energy bins can improve the reconstructions for the realistic data, and how performance varies with the number of energy bin.

Acknowledgment

This work was in part supported by the U.S. Department of Homeland Security. The views and conclusions contained in this document are those of the authors and should not be interpreted as necessarily representing the official policies, either expressed or implied, of the U.S. Department of Homeland Security.

References

[1] R. Ying, Zhengrong Naidu and C. R. Crawford, "Dual energy computed tomography for explosive detection," *Journal of X-ray Science and Technology*, vol. 14, no. 4, pp. 235–256, 2006.

[2] R. E. Alvarez and A. Macovski, "Energy-selective reconstructions in x-ray computerised tomography," *Physics in medicine and biology*, vol. 21, no. 5, p. 733, 1976.

[3] E. Roessl and C. Herrmann, "Cramér–rao lower bound of basis image noise in multiple-energy x-ray imaging," *Physics in medicine and biology*, vol. 54, no. 5, p. 1307, 2009.

[4] S. M. Kay, "Fundamentals of statistical signal processing, vol. 1: Estimate theory," *Signal Processing. Upper Saddle River, NJ: Prentice Hall*, 1993.

[5] G. Cowan, *Statistical data analysis*. Oxford University Press, 1998.

[6] O. Semerci, N. Hao, M. E. Kilmer, and E. L. Miller, "Tensor-based formulation and nuclear norm regularization for multienergy computed tomography," *Image Processing, IEEE Transactions on*, vol. 23, no. 4, pp. 1678–1693, 2014.

[7] C. Bouman, K. Sauer *et al.*, "A unified approach to statistical tomography using coordinate descent optimization," *Image Processing, IEEE Transactions on*, vol. 5, no. 3, pp. 480–492, 1996.

[8] W. C. Barber, E. Nygard, J. S. Iwanczyk, M. Zhang, E. C. Frey, B. M. Tsui, J. C. Wessel, N. Malakhov, G. Wawrzyniak, N. E. Hartsough *et al.*, "Characterization of a novel photon counting detector for clinical ct: count rate, energy resolution, and noise performance," in *SPIE Medical Imaging*. International Society for Optics and Photonics, 2009, pp. 725 824–725 824.